

Unveiling a Family of Dimerized Quantum Magnets, Conventional Antiferromagnets, and Nonmagnets in Ternary Metal Borides

Zhen Zhang,[#] Andrew P. Porter,[#] Yang Sun,* Kirill D. Belashchenko,* Gayatri Viswanathan, Arka Sarkar, Eranga H. Gamage, Kirill Kovnir,* Kai-Ming Ho, and Vladimir Antropov*



Cite This: *J. Am. Chem. Soc.* 2024, 146, 16878–16891



Read Online

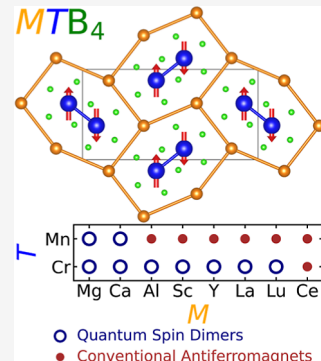
ACCESS |

Metrics & More

Article Recommendations

Supporting Information

ABSTRACT: Dimerized quantum magnets are exotic crystalline materials where Bose–Einstein condensation of magnetic excitations can happen. However, known dimerized quantum magnets are limited to only a few oxides and halides. Here, we unveil 9 dimerized quantum magnets and 11 conventional antiferromagnets in ternary metal borides MTB_4 ($M = Sc, Y, La, Ce, Lu, Mg, Ca, and Al; T = V, Cr, Mn, Fe, Co, and Ni$), where T atoms are arranged in structural dimers. Quantum magnetism in these compounds is dominated by strong antiferromagnetic (AFM) interactions between Cr (Cr and Mn for $M = Mg$ and Ca) atoms within the dimers, with much weaker interactions between the dimers. These systems are proposed to be close to a quantum critical point between a disordered singlet spin-dimer phase, with a spin gap, and the ordered conventional Néel AFM phase. They greatly enrich the materials inventory that allows investigations of the spin-gap phase. Conventional antiferromagnetism in these compounds is dominated by ferromagnetic Mn (Fe for $M = Mg$ and Ca) interactions within the dimers. The predicted stable and nonmagnetic (NM) $YFeB_4$ phase is synthesized and characterized, providing a scarce candidate to study Fe dimers and Fe ladders in borides. The identified quantum, conventional, and NM systems provide a platform with abundant possibilities to tune the magnetic exchange coupling by doping and study the unconventional quantum phase transition and conventional magnetic transitions. This work opens new avenues for studying novel magnetism in borides arising from spin dimers and establishes a theoretical workflow for future searches for dimerized quantum magnets in other families of materials.



INTRODUCTION

Quantum magnets have attracted great interest due to their many exotic phenomena.^{1,2} In quantum magnets, tuning the quantum phase transition across the quantum critical point (QCP) can lead to different novel states of matter. One of the simplest kinds of quantum magnets are those consisting of strongly coupled spin dimers. Antiferromagnetic (AFM) intradimer coupling results in a disordered quantum paramagnetic singlet ground state. Its first excited state is a triplet state. Interdimer interactions make the triplet bands dispersive.^{3,4} External parameters such as magnetic field,^{4–13} pressure,^{14–18} and doping^{19,20} have been shown to close the spin gap and generate magnetic order. Various descriptions for the ground state of the triplets, such as Bose–Einstein condensate,^{4,5,7–9,21} a triplet crystal,⁶ or a supersolid,¹⁰ have been proposed. Bose–Einstein condensation (BEC) of the bosonic triplons is a particularly interesting phenomenon² since BEC is well-known for its credit to the superconductivity of Cooper pairs and the superfluidity of 4He . In dimerized quantum magnets, at the QCP, the singlet ground state intersects the bottom of the lowest triplet's band dispersion, where BEC happens.⁴ Exploring novel quantum magnets and states of matter in the vicinity of the QCP is of great significance.

So far, dimerized quantum magnets have been discovered, and the associated BEC has been studied² mostly in oxides and halides such as $BaCuSi_2O_6$,^{4,8,9,22} $Ba_3Mn_2O_8$,^{11–13,23} and $TlCuCl_3$.^{5,7,14–19} Quantum spin dimers have yet been scarcely discovered and reported in boron compounds. Boron compounds are versatile due to their unusual electronic,²⁴ magnetic,^{24,25} and structural²⁶ properties. For example, boron nitride is a chemical analogue to carbon; both are expected to adopt similar one-, two-, and three-dimensional structures.²⁷ Borides are often reported to be suitable for high-temperature ferromagnets,^{28–31} catalysis,^{32–34} thermoelectricity,³⁵ and superhard materials.^{36–39} Superconductivity has been discovered in magnesium diboride (MgB_2).^{40–43} $Nd_2Fe_{14}B$ is one of today's best-performing permanent magnets.⁴⁴ The formation of binary, ternary, and multinary borides among boron and metal elements provides a rich materials family to explore.

Driven by the idea to seek quantum spin dimers in borides, we uncover the family of compounds with a $YCrB_4$ -type

Received: April 22, 2024

Revised: May 21, 2024

Accepted: May 23, 2024

Published: June 4, 2024



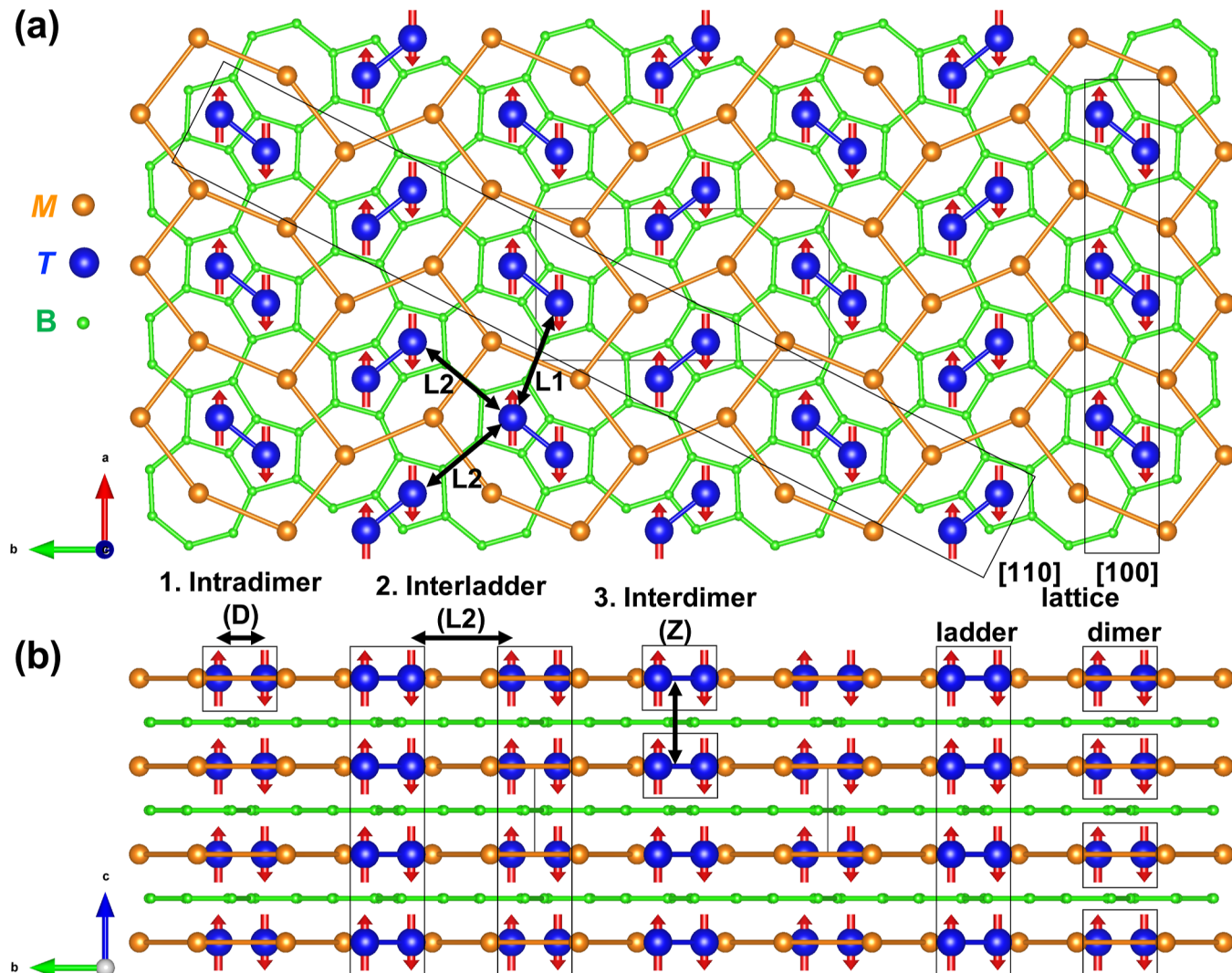


Figure 1. YCrB_4 -type crystal structure. (a) [001] and (b) [100] projections. Orange, blue, and green spheres show M, T, and B atoms, respectively. Red arrows show magnetic moments. AFF magnetic ordering is displayed in the figure as an example. The three-letter notation for the magnetic configuration indicates the relative alignment of the local moments inside a dimer (D), between the nearby dimers in the same plane (L2), and between the neighboring layers (Z).

structure. YCrB_4 was reported to offer promising physical properties such as thermoelectricity^{45,46} and high mechanical strength.^{47–49} This class of materials, i.e., metal (M)–transition metal (T)–tetraborides (B_4), was reported by early experimental studies.^{50,51} ScTB_4 (T = Fe, Co, and Ni), YTB_4 (T = V, Cr, Mn, Fe, and Co), CeTB_4 (T = Cr, Mn, Fe, and Co), and LuTB_4 (T = Cr, Fe, Co, and Ni) were briefly mentioned.^{50–54} However, methods to produce single-phase samples suitable for characterization are known only for a subset of the reported compounds. On the other hand, theoretical investigations of the fundamental electronic and magnetic properties of these compounds are scarce, even for the prototypical YCrB_4 .^{46,47,55} Previous first-principles calculations for YCrB_4 show nonmagnetic (NM)^{46,47} and semiconducting^{46,47,55} behavior. A remarkable structural feature of this class of materials is a transition-metal dimer formation. How such a transition-metal dimer formation quantum-mechanically impacts the materials' electronic and magnetic properties is unknown and to be explored.

In this study, we utilize first-principles calculations to study the electronic and magnetic properties of MTB_4 , where M is

IIIB metals (Sc, Y, La, Ce, and Lu) and T is 3d transition metals (V, Cr, Mn, Fe, Co, and Ni). The NM IIIB elements are considered to eliminate the magnetic effects arising from the M atoms on the transition-metal dimers. Sc, Y, La, and Lu have similar valence shell structures; thus, their formed MTB_4 compounds are expected to show similar physical properties. Our previous study⁵⁶ generalized M in this class of materials to the main-group elements, Mg, Ca, and Al. However, whether they are quantum magnets remains to be studied. In this work, we investigate the quantum magnetism for this entire generalized family of materials.

Note that there are other RTB_4 compounds⁵² adopting the same YCrB_4 -type structure, where R is the rest of the rare-earth elements with a partially filled f shell and usually expected to be magnetic. The magnetic R element forming squashed hexagons outside the T dimers may change the magnetic behaviors of the T dimers. Thus, these compounds are not included in this study. These RTB_4 compounds, when R is magnetic, can exhibit a variety of interesting magnetic phenomena or transitions. For instance, YbNiB_4 exhibits strong Kondo

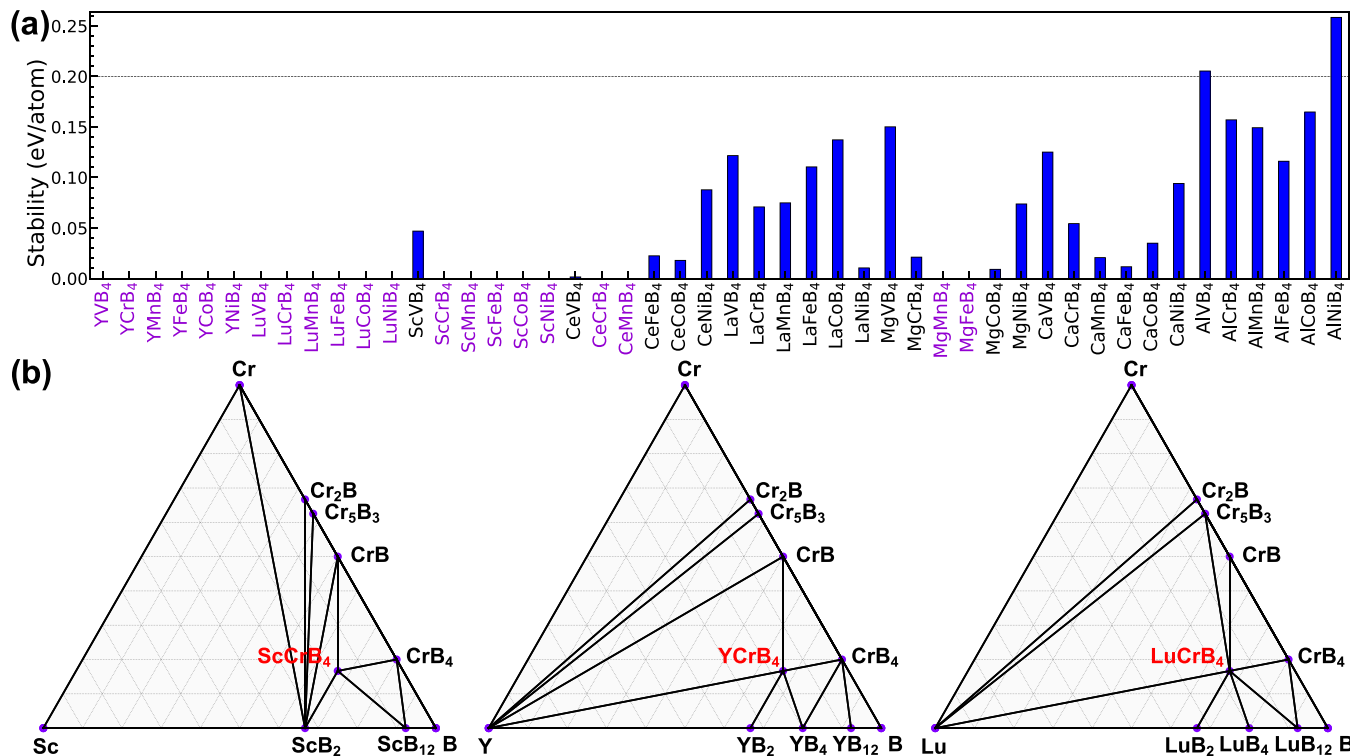


Figure 2. Phase stability. (a) Stability of YCrB_4 -type MTB_4 . Purple compositional x -labels indicate stable compounds. (b) Convex hulls for $\text{M}-\text{Cr}-\text{B}$ ($\text{M} = \text{Sc}, \text{Y}$, and Lu).

interaction with additional low-dimensional AFM fluctuations.⁵⁷

From the synthesis point of view, YCrB_4 is the compound that gives the name to this structure type. YCrB_4 and YMnB_4 have been experimentally studied, and their crystal structures were reported together with some conventional properties.^{45,46,49–51} In turn, YFeB_4 and YCoB_4 have been only briefly mentioned without properly describing the experimental synthetic procedures. In this study, experimental efforts are focused on the synthesis of YFeB_4 and YCoB_4 and the characterization of their structure and basic properties. Synthetic and computational approaches were developed in parallel in this work to further future studies of abundant quaternary borides containing two IIIB metals or two 3d metals, i.e., doping on the M site or the T site.

RESULTS AND DISCUSSION

YCrB_4 -Type Crystal Structure. The YCrB_4 -type crystal structure is displayed in Figure 1. It crystallizes in the $Pbam$ space group with a layered structure, consisting of alternating sheets of boron atoms and metal atoms. The sheet of boron atoms forms a tiling of pentagons and heptagons. The sheet of metal atoms consists of a tiling of squashed hexagons of M atoms with a transition-metal dimer inside each hexagon. Take YTB_4 , for example. The intradimer distances (D) are ~ 2.3 – 2.6 Å for different T elements. Dimers form ladders in the direction perpendicular to the plane ([001]). Dimer–dimer separation along the ladder (Z) is $\sim 1.4 D$. Ladders make up a two-dimensional lattice in directions parallel to the plane ([110], [1 $\bar{1}$ 0], or [100]). Ladder–ladder separation (L_1, L_2) is $\sim 2 D$. (Each T atom has one L1 and two L2 neighbors at very similar distances.) Since the intradimer distance is the

shortest among the three, intradimer interaction should be the strongest interaction among the T atoms.

Phase Stability. The formation energy (E_{form}) is obtained from spin-polarized calculations. Then, the formation energy relative to the convex hull (E_d) is evaluated by the formation energy differences with respect to the three reference phases forming the Gibbs triangle on the convex hull. The reference phases on the convex hulls are obtained from materials databases such as Materials Project⁵⁸ and OQMD.⁵⁹ All phases are fully relaxed, and the total energies are calculated using the same density-functional theory (DFT) settings. If an MTB_4 phase has $E_d < 0$, then it is stable. In this case, the convex hull is reconstructed to include the MTB_4 's E_{form} , and the MTB_4 's stability is denoted as zero. If an MTB_4 phase has $E_d > 0$, then it is not stable. In this case, the MTB_4 's stability indicates the distance above the convex hull. The calculated stabilities of all MTB_4 are shown in Figure 2a. Stability = 0 indicates a stable phase. We use 0.2 eV/atom⁶⁰ as the criterion for choosing metastable compounds that are possibly stabilized by thermodynamics. Then, we obtain 21 stable and 25 metastable compounds in MTB_4 . The calculated convex hulls for $\text{M}-\text{Cr}-\text{B}$ ($\text{M} = \text{Sc}, \text{Y}$, and Lu) systems are exhibited in Figure 2b.

Note that apart from the YCrB_4 -type α phase, there is also a very similar ThMoB_4 -type β phase ($Cmmm$ space group). The β phase also consists of alternating sheets of boron atoms and metal atoms. Its metal layer also consists of transition-metal dimers but with a different arrangement from that in the α phase. Both phases have been found in RAIB_4 (R = rare earth) compounds such as YbAlB_4 .⁶¹ The comparison of energetics between these two phases is shown in Figure S1 of the Supporting Information. The α phase studied here is more stable than the β phase for most (43/48) of the MTB_4 compounds in this work. There are 5 compounds, CeFeB_4 ,

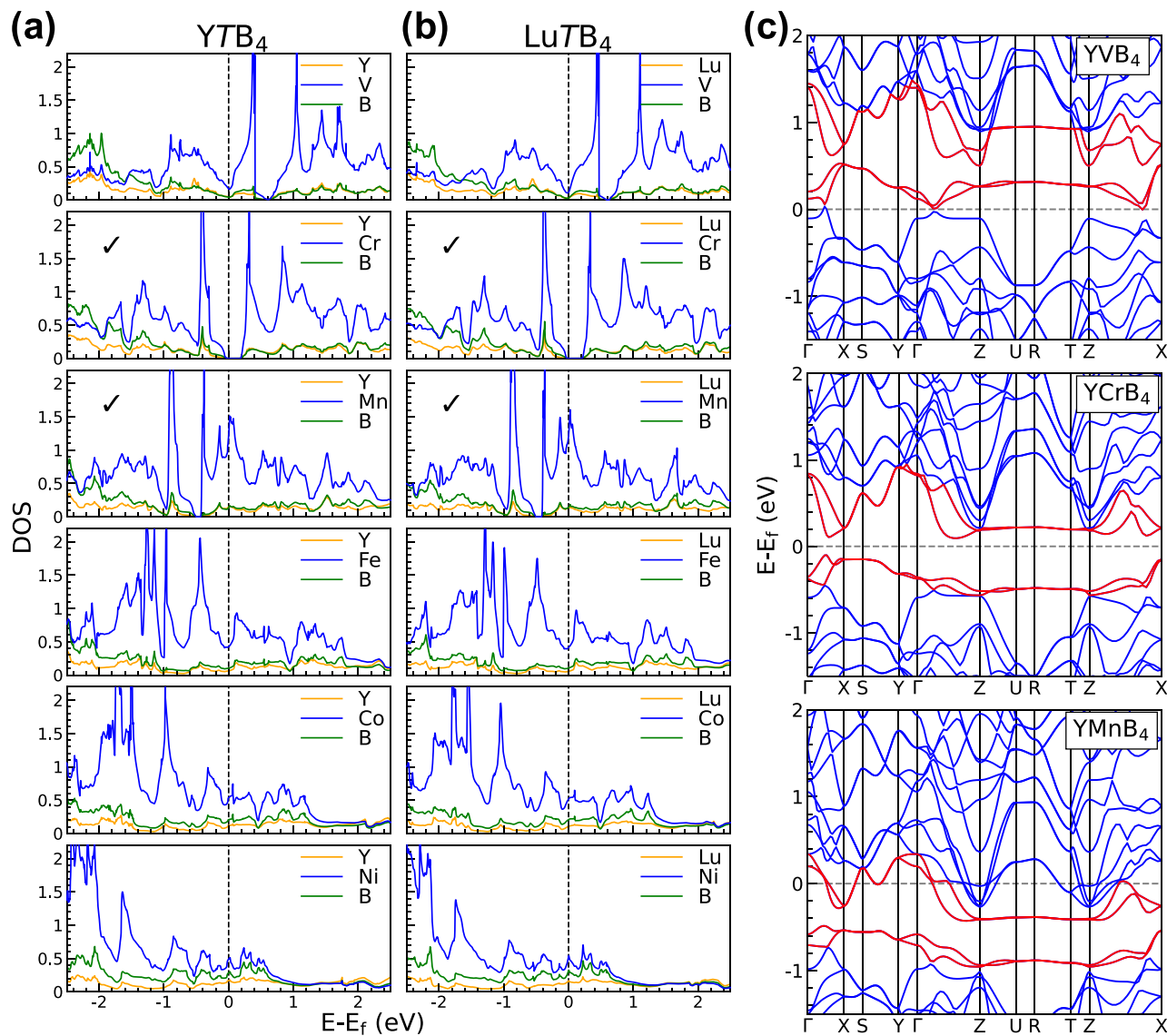


Figure 3. NM electronic structures. DOS ($\text{eV}^{-1} \text{f.u.}^{-1} \text{spin}^{-1}$) for (a) YTB_4 and (b) LuTB_4 ($T = \text{V, Cr, Mn, Fe, Co, and Ni}$). Orange, blue, and green curves represent partial DOS of M, T, and B atoms, respectively. Check marks indicate systems with stable magnetic solutions. (c) Band structure for YTB_4 ($T = \text{V, Cr, and Mn}$). High-symmetry points in the Brillouin zone are denoted as follows: $\Gamma(0, 0, 0)$, $X(1/2, 0, 0)$, $S(1/2, 1/2, 0)$, $Y(0, 1/2, 0)$, $Z(0, 0, 1/2)$, $U(1/2, 0, 1/2)$, $R(1/2, 1/2, 1/2)$, $T(0, 1/2, 1/2)$. Red color highlights nearly flat bands in the Brillouin zone corresponding to two narrow peaks in the NM DOS.

LaMnB_4 , LaFeB_4 , LaCoB_4 , and LaNiB_4 , for which the β phase is more stable.

Nevertheless, these five compounds are metastable, and the energy differences between the two phases are much smaller than the convex hull distances presented in Figure 2a. According to the summary of early experimental results,⁵² the α phase of CeFeB_4 exists instead of the β phase.

Electronic Properties of the NM States. The NM density of states (DOSs) for the representative Y and Lu compounds are plotted in Figure 3, and the DOSs at the Fermi level $N(E_f)$ are listed in Table 1. Due to limited space, our discussion will mainly focus on Y compounds. Other compounds have been analyzed similarly. $N(E_f)$ of these compounds is mainly contributed by the T atom. V has a low DOS at the Fermi level, making V compounds weakly metallic. Fe, Co, and Ni have $N(E_f) \sim 0.5 \text{ eV}^{-1} \text{f.u.}^{-1} \text{spin}^{-1}$. Hence, these compounds are “good” metals. For Fe, the Fermi level is at the minimum of DOS, but there is a peak right above it.

Table 1. DOS of Transition Metals $N_T(E_f)$ ($\text{eV}^{-1} \text{f.u.}^{-1} \text{spin}^{-1}$) and Total DOS $N_{\text{tot}}(E_f)$ ($\text{eV}^{-1} \text{f.u.}^{-1} \text{spin}^{-1}$) at the Fermi Level for YTB_4 and LuTB_4

compound	$N_T(E_f)$	$N_{\text{tot}}(E_f)$	compound	$N_T(E_f)$	$N_{\text{tot}}(E_f)$
YVB_4	0.165	0.331	LuVB_4	0.117	0.230
YCrB_4	0.0	0.0	LuCrB_4	0.0	0.0
YMnB_4	1.209	1.696	LuMnB_4	1.194	1.656
YFeB_4	0.425	0.680	LuFeB_4	0.417	0.667
YCoB_4	0.537	1.016	LuCoB_4	0.516	0.972
YNiB_4	0.488	1.142	LuNiB_4	0.530	1.210

Applying some strain or doping may move the Fermi level toward this peak. For Ni, the Fermi level is located at a minor peak. In contrast, for Mn, the Fermi level is at a sharp peak of DOS, suggesting a strong electronic instability.

The NM DOS for YCrB_4 shows a semiconducting character with a narrow band gap of 0.20 eV, which agrees with the

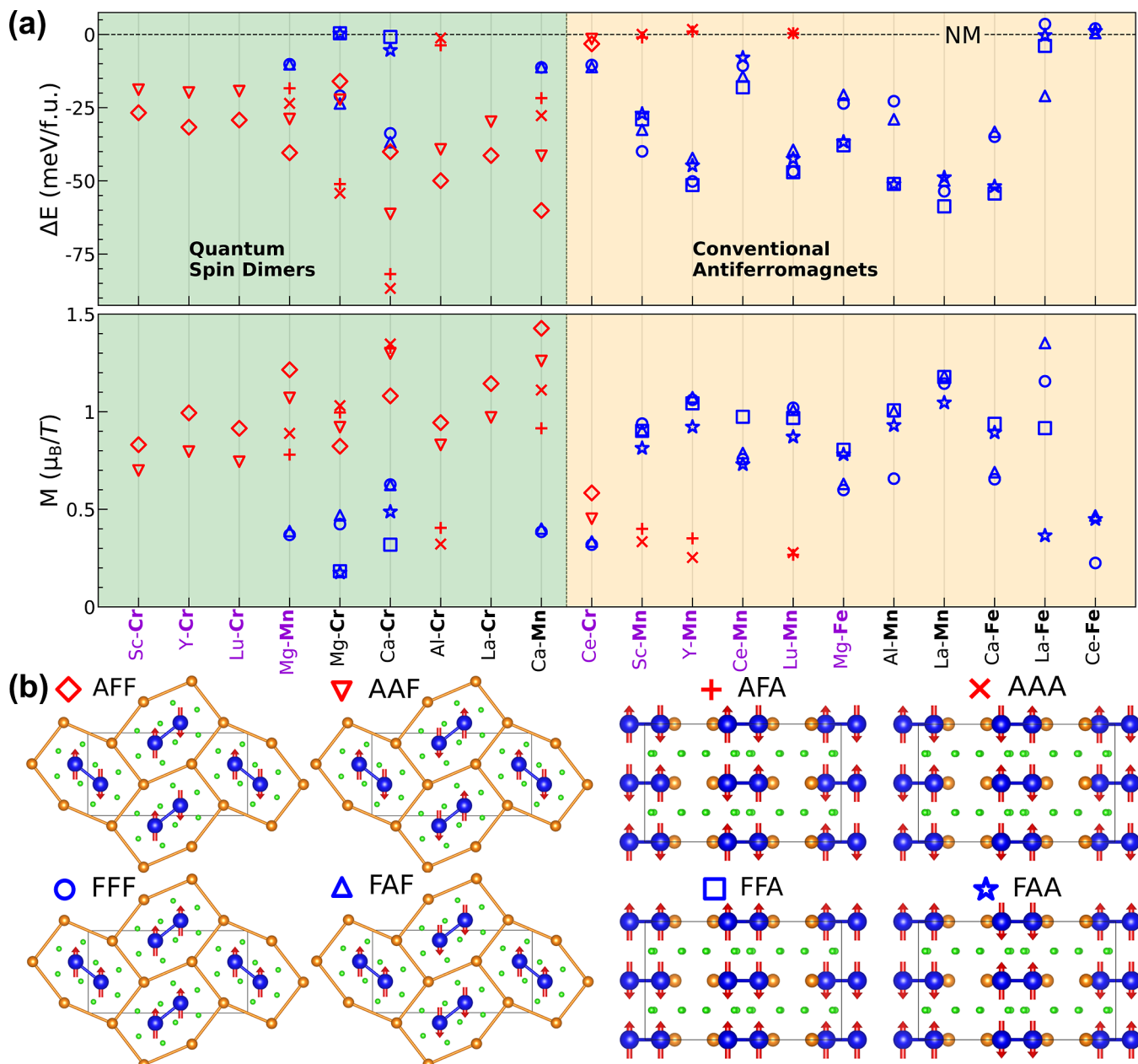


Figure 4. DFT magnetic solutions. (a) Relative energy difference of the magnetic solutions to the NM one (top) and the magnetic moment on the transition metal T (bottom) for MTB₄. The green and orange regions indicate quantum spin dimers and antiferromagnets, respectively. Purple and black compositional x-labels indicate stable and metastable compounds, respectively. (b) Different magnetic configurations and the associated symbols.

experimental estimate of 0.17 eV.⁴⁵ The semiconducting character of NM YCrB₄ agrees with previous first-principles calculations,^{46,47,55} which reported a gap of 0.05,⁵⁵ 0.14 ± 0.04,⁴⁶ and 0.17 eV.⁴⁷

A remarkable feature in the NM DOS of these compounds is the presence of two narrow peaks, both of which are empty in V, straddle the Fermi level in Cr, and are filled in Mn compounds. These narrow peaks displayed in the electronic spectrum are known as Van Hove singularities (VHS). Generally, VHS near the Fermi level can lead to instabilities, such as charge density waves, and induce phase transitions under changing temperature, pressure, or chemical doping. They can also be associated with interesting optical properties and with large DOS near the Fermi level, the latter of which

tends to enhance superconductivity. Understanding the presence and influence of VHS is valuable in the design and engineering of new materials.

These VHS result from two pairs of bands, highlighted in red in Figure 3, that are nearly flat on the $k_z = 1/2$ plane (Z–U–R–T–Z path in Figure 3). The flat bands are formed by d_{z^2} orbitals of the transition-metal atoms,⁴⁶ and the two pairs of bands correspond to bonding and antibonding states of the dimers. (Two bands in each pair correspond to two dimers per unit cell.) For a generic wavevector, the dimer states can hybridize with B atoms, leading to significant dispersion visible along the Γ –X–S–Y– Γ –Z path. However, this hybridization is suppressed at $k_z = 1/2$ due to the destructive interference between the hopping amplitudes for the two transition-metal

sheets to the s, p_x , and p_y orbitals of the B atoms. This cancellation effectively localizes the dimer states with $k_z = 1/2$, leading to flat bands and the corresponding peaks in the DOS. The strength of the interdimer hybridization determines the width of the peaks and is, therefore, much smaller (at about 0.2 eV for Cr compounds) than in Cr metal, where it is in the range of 1–2 eV.

The DOS for the different transition metals exhibits an approximately “rigid band” behavior. By tuning electron concentration and changing the transition metal from V to Mn, the DOS plots show similar patterns with the Fermi level located below, in between, and above the two major VHS, respectively. Such a “rigid band” behavior is common for similar systems.⁵⁶

Magnetic States. VHS near the Fermi level may be associated with various electronic instabilities. Based on the analysis of the real-space paramagnetic Pauli spin susceptibility matrix (see Section Methods), we consider magnetic orderings with ferromagnetic (FM) or AFM alignment of the local moments within a dimer (1. intradimer), between the nearby dimers in the same plane (2. interladder), and between the adjacent layers (3. interdimer) as shown in Figure 1. We will use a three-letter notation consisting of letters F (for FM) and A (for AFM) to denote these orderings, such as AFF, where each letter identifies the alignments in this particular order. The labeling of the first and the third letters is straightforward. A few comments are in order about the in-plane interladder ordering, which is indicated by the second letter. (i) It indicates the ordering between dimers along the L2 but not L1 direction (see Figure 1). (ii) The alignment is identified by comparing spins between DL2, which is the linked path of D and L2. (iii) The A ordering is similar to the stripe ordering on the hexagonal lattice. The specific ordering patterns are displayed in Figure 4.

Eight magnetic configurations are obtained through all possible combinations of these alignments and are considered in the calculations. For example, AFF means intradimer AFM, interladder FM, and interlayer FM coupling. The AFF configuration is displayed in Figure 1. However, not all of these configurations are stable; many do not have a self-consistent DFT solution with finite magnetic moments.

Figure 4a shows all the stable magnetic solutions for MTB₄, with the eight magnetic configurations illustrated in Figure 4b. The top panel of Figure 4a shows the stabilization energy relative to the NM state, and the bottom panel shows the magnetic moment on the T atoms. Compounds without any magnetic solutions are not shown. In total, we find 20 magnetic compounds, among which 10 are stable (purple composition labels) and 10 are metastable (black composition labels) as shown in Figure 4a. Strong AFM intradimer exchange and weak interdimer interactions result in quantum spin-gap systems. According to the alignment of intradimer coupling of the DFT ground state, we group these compounds into two categories: quantum spin-dimer magnets and conventional magnets (see Figure 4). Such categorization immediately justifies itself. It is clear that the DFT ground state always has the same intradimer spin alignment, indicated by the symbol color, as those of multiple low-energy states. Such a phenomenon results from the dominating intradimer coupling strength compared to the interdimer ones. Dimerized quantum magnets exhibit AFM intradimer spin alignments (red symbols in Figure 4) as DFT ground state and low-energy states, while

conventional magnets exhibit FM intradimer spin alignments (blue symbols) as ground and low-energy states.

We identify a total of 9 quantum spin-dimer magnets and 11 conventional magnets. Note that although the ground states of the conventional magnets have FM intradimer ordering, they are still overall AFM with zero net spins. The only exception is ScMnB₄, the ground state of which is overall FM (FFF). Considering the closeness of its energy to other AFM states, we do not specifically distinguish this one and denote all the conventional magnets as conventional antiferromagnets. Remarkably, compounds with the same valence shell electron count belong to the same magnet category and exhibit a similar distribution of magnetic solutions. Cr forms a quantum AFM dimer with two ordered solutions when combined with Sc, Y, La, and Lu. Mn forms a conventional FM dimer with four well-defined magnetic solutions when combined with Sc, Y, La, and Lu. V, Fe, Co, and Ni are NM when combined with these IIIB elements. Accordingly, the IIIA element Al makes Cr quantum and Mn conventional with similar distributions of magnetic solutions. Analogously, when it comes to IIA elements Mg and Ca, Mn and Fe play the same role as Cr and Mn, respectively, for the group III elements. Therefore, Mn forms quantum spin dimers when combined with Mg and Ca, and Fe forms FM spin dimers with Mg and Ca. In turn, Cr plays the same role as V but is not as silent as V. Cr forms extra quantum spin dimers when combined with Mg and Ca. In case of Ce, it is more complicated due to 4f electron localization issues. Hubbard U may be required, which may change the current results for Ce. We leave this to future study and only report Ce’s magnetism by generalized gradient approximation (GGA) here.

The reliability of our prediction of magnetism in these compounds is justified from the following two perspectives. (i) The addition of Hubbard U increases the magnetic moments in the studied compounds. The magnetic states reported here become even more stable with the resulting increase in magnetic energy. We do not see any signs of magnetism weakening when the Hubbard U is added. In particular, YCrB₄ retains the AFM dimer ground state. The resulting energy gap is not increasing, supporting the semiconducting behavior identified theoretically and observed experimentally. Thus, GGA + U calculations support our current GGA predictions. However, we need more information about the strength of electronic correlations in these materials, and we cannot use GGA + U calculations to predict, for instance, the amplitude of local moments. (ii) It is known that GGA tends to give larger local moments compared to local density approximation (LDA). LDA calculations of these magnetic compounds yield smaller yet still significant moments. Thus, magnetism is also stable in LDA.

Next, we analyze the magnetic solutions for the representative Y and Lu compounds in detail. Earlier calculations predicted these systems to be NM.^{46,47} However, we find the DFT ground states to be AFF for Cr and FFA for Mn. In their respective DFT ground states, the magnetic moments on Cr and Mn atoms are close to 1 μ_B . Besides the ground states, self-consistent magnetic solutions were found in Cr and Mn compounds with AAF ordering for Cr and FFF, FAF, FAA, AFA, and AAA orderings for Mn. Among these, the AFA and AAA solutions for Mn have small magnetic moments of about 0.3 μ_B and the total energies are very close to the NM solution. It may indicate a weak magnetic moment dependence for the energy surface near the NM state, which could enhance magnetic fluctuations.

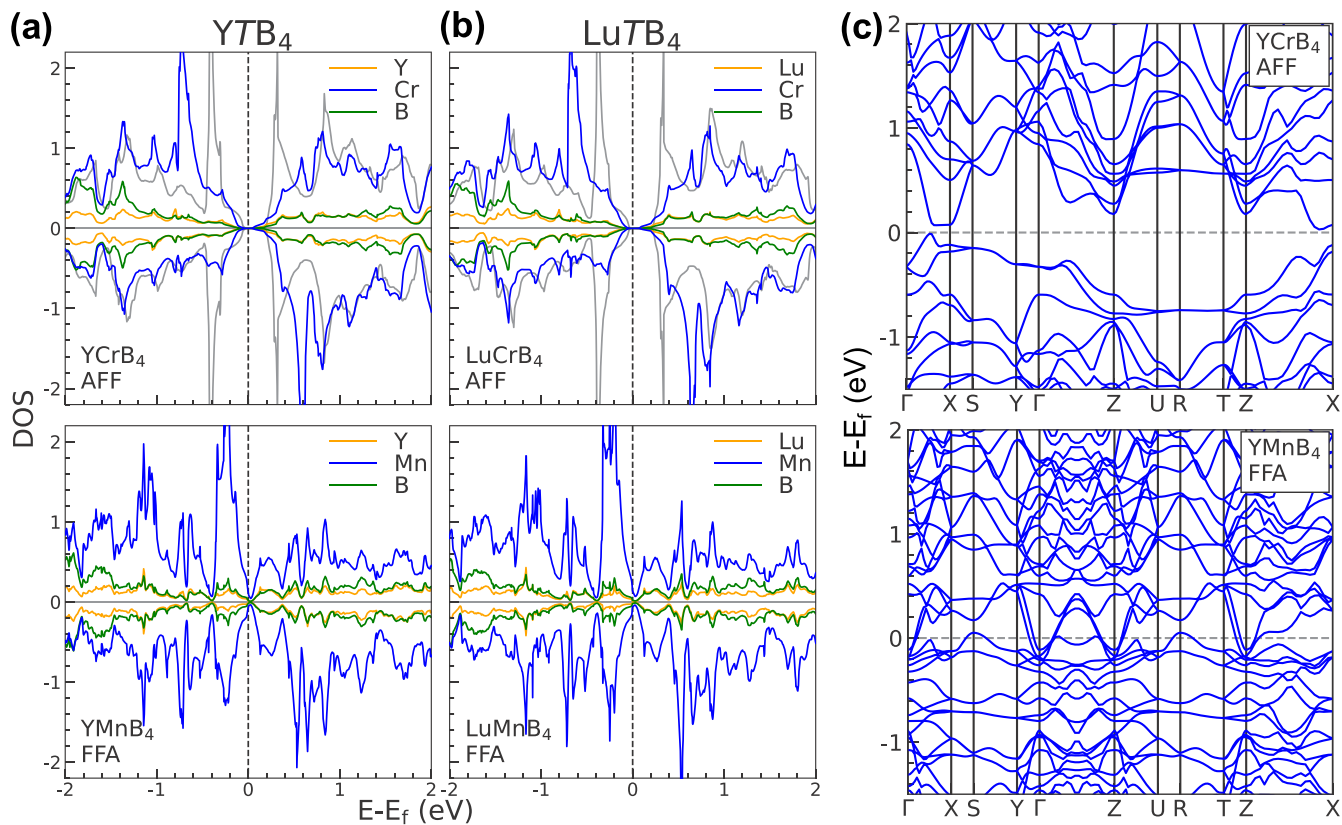


Figure 5. Magnetic electronic structures. The partial spin-polarized DOS (in eV^{-1} f.u.⁻¹ spin⁻¹) of the DFT ground state of (a) YTB_4 and (b) LuTB_4 . T = Cr has AFF solution, and T = Mn has FFA solution. Positive (negative) DOS indicates majority (minority) spin. The corresponding NM partial DOS for a Cr atom is displayed as gray curves for comparison. (c) Spin-polarized electronic band structure for the magnetic ground-state YCrB_4 (top) and YMnB_4 (bottom).

Focusing on the solutions with well-defined magnetism, YMnB_4 has stable magnetic solutions in all configurations with FM intradimer alignment (FFF, FAF, FFA, and FAA), which all have similar energies (42–51 meV/f.u. below the NM solution) and local moments close to $1 \mu_\text{B}$. This reflects the small scale of the interdimer exchange coupling compared to the intradimer coupling. AFM interlayer orderings, FFA and FAA, are more stable than FM interlayer orderings, FFF and FAF, by 1.2 and 2.6 meV/f.u., respectively. FM interladder orderings, FFF and FFA, are more stable than AFM interladder orderings, FAF and FAA, by 8.0 and 6.6 meV/f.u., respectively. On the other hand, YCrB_4 has only two stable magnetic solutions, AFF and AAF, which have AFM intradimer spin alignment and energies 32 and 20 meV/f.u. below the NM solution, respectively. Interestingly, Cr only has AFF and AAF solutions, indicating stable spin ladders with in-plane moment disorder with a significant energy separation of 11.9 meV/f.u. This energy is like that for YMnB_4 (8.0 and 6.6 meV/f.u.) but slightly larger. These observations for the Y compounds also apply to the Lu compounds.

The three typical T–T distances for the NM and DFT ground-state magnetic solutions are displayed in Figure S2 of the Supporting Information. For the NM states, D, L2, and Z show nonmonotonic trends with varying 3d transition metals. For the magnetic states of the Cr and Mn systems, Z is insensitive to magnetism, whereas D is increased, and L2 is slightly decreased by magnetism. D of both AFM Cr dimers and FM Mn dimers is longer than their respective NM ones by $\sim 0.04 \text{ \AA}$. This suggests that the intradimer exchange coupling

in both Cr and Mn compounds is strengthened when the intradimer bond length increases, which is somewhat unusual. Note that the T–T distances for different stable magnetic solutions agree with the DFT ground-state ones and those for the two marginally stable AFA and AAA solutions for Mn are similar to those for the NM solution. Therefore, only DFT ground states of the magnetic solutions are shown.

We now examine the electronic properties of the DFT ground states. Figure 5 displays the spin-polarized DOS for the ground-state AFF Cr and FFA Mn compounds. The results for the Y and Lu compounds are very similar. AFF-ordered YCrB_4 is a magnetic semiconductor with a small band gap of 0.05 eV. Compared to the NM partial DOS of a Cr atom, which is shown in gray in Figure 5, the peaks in the magnetic DOS are shifted by about 0.3 eV. FFA- YMnB_4 is a “bad” magnetic metal with a low total DOS of 0.13 eV^{-1} f.u.⁻¹ spin⁻¹ at the Fermi level. While Mn atoms are aligned ferromagnetically in each layer, different layers align antiferromagnetically along the z-direction. The spin-polarized band structures for the ground-state AFF- YCrB_4 and FFA- YMnB_4 are displayed alongside the DOS in Figure 5.

The DFT ground states are either semiconducting or weakly metallic for MTB₄ (M = Y and Lu). The semiconducting Cr compounds in the NM state^{46,47,55} remain semiconducting in the magnetic state. In contrast, a change from a good metal to a bad metal is seen in Mn compounds when they switch from NM to magnetic. Considering that conventional DFT functionals such as LDA and GGA tend to underestimate the band gap, the band gaps in Cr compounds are expected to

Table 2. Exchange Parameters J_{ij} (in mRy) in Magnetic MTB_4 ($\text{M} = \text{Y}$ and Mg)

pair	N_j	AFF-YCrB ₄		FFA-YMnB ₄		AAA-MgCrB ₄		AFF-MgMnB ₄		FFA-MgFeB ₄	
		R_{ij}	J_{ij}	R_{ij}	J_{ij}	R_{ij}	J_{ij}	R_{ij}	J_{ij}	R_{ij}	J_{ij}
D	1	2.36	-2.2	2.44	2.00	2.35	-1.40	2.40	-1.36	2.42	0.94
Z	2	3.44	0.26	3.42	-0.09	3.25	-0.02	3.19	0.15	3.18	-0.15
DZ	2	4.17	-0.40	4.20	0.08	4.01	0.52	3.99	-0.17	4.00	-0.14
L1	1	4.83	-0.02	4.79	0	4.73	-0.03	4.70	0.004	4.67	0.02
L2	2	4.89	-0.03	4.81	-0.01	4.79	0.03	4.73	-0.03	4.69	-0.02
DL1	2	5.93	0	5.90	0.09	5.85	-0.06	5.83	0.02	5.79	0.09
DL2	2	5.93	-0.01	5.89	0.08	5.80	-0.06	5.76	-0.03	5.73	0.04
ZL1	2	5.93	-0.15	5.88	-0.03	5.74	-0.08	5.68	-0.11	5.65	0
ZL2	4	5.98	-0.11	5.90	-0.03	5.79	-0.06	5.71	-0.10	5.66	-0.01
J_0			4.54		2.59		2.94		2.49		1.98
M			1.01		0.91		1.00		0.93		0.68
J_D/J_0			-0.48		0.77		-0.48		-0.55		0.47
$ J'_0/J_D $			1.06		0.29		1.10		0.83		1.11

be more significant. Mn compounds can also be magnetic semiconductors. These materials are band semiconductors or metals but not charge-transfer insulators. The magnetic moment of about $1 \mu_B$ in the DFT ground states suggests the spin-1/2 state of the T atom in these magnetic compounds.

Furthermore, we calculate the exchange coupling parameters in the DFT ground states of MTB_4 using the linear response technique⁶² implemented within the tight-binding linear muffin-tin orbital (TB-LMTO) method in the Questaal code.⁶³ For YCrB₄, we note that the magnetic moment on the Cr atoms is sensitive to computational details and is too small at $0.49 \mu_B$ in LMTO compared to the full-potential VASP calculation ($0.99 \mu_B$). We correct this discrepancy by scaling the exchange-correlation field by a factor of 1.13, which increases the magnetic moment to $1.01 \mu_B$. Similarly, for MgCrB₄, the exchange-correlation field is scaled by 1.19 to obtain the local moment of $1.00 \mu_B$. For YMnB₄, MgMnB₄, and MgFeB₄, the local magnetic moment in the ground state in LMTO is 0.91 , 0.93 , and $0.68 \mu_B$, respectively.

The calculated exchange parameters are listed in Table 2. The parameters are defined as the effective Heisenberg model, $E = -\sum_{ij} J_{ij} \hat{m}_i \hat{m}_j$, where each atomic pair is counted twice, and \hat{m}_i are unit vectors showing the direction of magnetization for magnetic atom i . Positive (negative) exchange parameters correspond to FM (AFM) coupling. Antiparallel pairs are highlighted in bold. N_j : number of neighbors of a given type. R_{ij} (in Å): distance to the given neighbor. D: dimer pair. Z: nearest neighbor along the c axis. DZ: the nearest neighbor along the c axis of the D neighbor. L1 and L2: two inequivalent neighbor types between the nearest ladders. A combination of symbols designates links of a path to the other site. $J_0 = \sum_j J_{ij} \hat{m}_i \hat{m}_j$ is the total exchange coupling between a given site and the rest of the crystal. M (in μ_B) is the local moment in LMTO. J'_0 is similar to J_0 but excludes the contribution from the D neighbor.

The nearest-neighbor intradimer exchange coupling (denoted as D) is dominant and quite strong in both YCrB₄ and YMnB₄. This intradimer exchange coupling is AFM in YCrB₄ and FM in YMnB₄, consistent with the magnetic ground states determined above based on total energy calculations. The signs of all significant exchange parameters listed in Table 2 for YCrB₄ agree with their relative alignment in the ground state, indicating the absence of any magnetic frustration. In YMnB₄,

only the weak DZ and L2 couplings are frustrated among those listed in Table 2.

The last line in Table 2 lists the $|J'_0/J_D|$ ratio, where J'_0 is the total exchange coupling of a given magnetic moment to the rest of the lattice, excluding its D neighbor. This ratio is 1.06 in YCrB₄ and only 0.29 in YMnB₄. Because the total coupling with other dimers is at most comparable with intradimer coupling, the spins of the dimer partners should be strongly correlated in the interesting temperature range where a magnetic phase transition is possible. For YMnB₄ with FM intradimer coupling and much weaker coupling to the rest of the lattice, it is reasonable to assume that each dimer is maximally correlated, i.e., consider it a composite entity with effective spin 1. Because the frustrated DZ and L2 couplings only amount to 15% of J'_0 , the effect of this frustration on magnetic thermodynamics should be negligible. Examination of the exchange parameters in YMnB₄ also shows that the coupling has a three-dimensional character; neither the interlayer nor interladder coupling is anomalously small.

Because the exchange coupling between dimers in YMnB₄ is three-dimensional without significant frustration, it is expected to order antiferromagnetically at a temperature that may be estimated using the mean-field approximation. The total coupling of a dimer to the rest of the crystal is $2J'_0$. Treating the spins classically, we obtain $T_N \sim (2/3)2J'_0/k_B \approx 120 \text{ K}$.

Now consider YCrB₄, where strong AFM intradimer coupling favors the formation of a singlet spin-gap state with no magnetic order.^{64,65} The singlet spin-gap state competes with the antiferromagnetically ordered state favored by exchange coupling between the dimers. Proceeding similarly to ref 65, we consider a Heisenberg lattice spin-1/2 Hamiltonian where interaction between dimers will be treated on the mean-field level, while the 4×4 Hamiltonian of a given dimer will be diagonalized exactly. In this dimer Hamiltonian, interactions with other dimers are represented by effective fields obtained by replacing the spin operators for other dimers by their expectation values. The solution of this quantum mean-field model predicts a QCP between the singlet spin-gap and the magnetically ordered state at $|J'_0/J_D| = 1$. With $|J'_0/J_D| = 1.06$, YCrB₄ is thus expected to be close to the QCP.

Experimental measurements show that YCrB₄ has a very small magnetic susceptibility, which was attributed to a small concentration of magnetic impurities.⁴⁶ In dimerized spin-gap systems, the magnetic susceptibility is suppressed at temperatures that are small compared to the singlet-triplet energy

gap.^{66–68} In the mean-field approximation for the interaction between quantum spin-1/2 dimers, the susceptibility is^{66–69}

$$\chi = \frac{k_B C}{k_B T \left(\frac{3}{4} + \frac{1}{4} \exp(2\beta |J_D|) \right) + 2J'_F} \quad (1)$$

where it is assumed that $J_D < 0$, C is the Curie–Weiss constant, and $J'_F = \sum_j J_{ij}$ with J_D excluded.

Using $J_D = -2.2$ mRy from Table 2, we can estimate the singlet–triplet splitting for the isolated dimer Hamiltonian $H_D = -2J_D \hat{\sigma}_1 \hat{\sigma}_2$ as $2|J_D| = 4.4$ mRy. (We assume the DFT calculations correspond to mean-field energies $E_D = -2J_D \hat{m}_1 \hat{m}_2$.) This corresponds to a temperature of order 700 K, below which the magnetic susceptibility should be suppressed due to the formation of a spin gap.

Exchange parameters for Mg compounds are also listed in Table 2. Mg has a different valence shell electron count from Y. Two quantum spin-dimer magnets, MgCrB_4 and MgMnB_4 , have relatively weaker J_D , -1.40 and -1.36 mRy, respectively, compared to that of YCrB_4 . Thus, the spin gaps are expected to cause a suppression for the magnetic susceptibility below a temperature of around 450 K. Nevertheless, due to a relatively weaker J'_0 , MgCrB_4 and MgMnB_4 produce similar $|J'_0/J_D|$ ratios to that of YCrB_4 , 1.10 and 0.83, respectively, and thus are also expected to be close to the QCP.

As for the conventional antiferromagnet, MgFeB_4 , the frustrated L2 coupling only contributes to 2% of J'_0 . Hence, the effect of frustration is weaker than the one for YMnB_4 . On the other hand, the $|J'_0/J_D|$ ratio of MgFeB_4 is significantly larger than that of YMnB_4 due to MgFeB_4 's much weaker intradimer coupling and stronger coupling of a dimer to the rest of the crystal. We further estimate $T_N \sim 220$ K, again, as in the case of YMnB_4 , considering the dimer to be rigidly coupled.

By alloying the dimerized quantum magnets with different T elements on the T sublattice or with different M elements on the M sublattice, it may be possible to tune the exchange coupling across the QCP, providing a rare platform and abundant candidates for studying the spin-gap QCP.

Experimental Synthesis. The synthesis and basic properties of YCrB_4 and YMnB_4 borides have already been reported. In turn, for YFeB_4 and YCoB_4 , the formation of the phases was mentioned, but neither the procedure to produce single-phase samples nor properties were reported.^{45,46,49–51} Our experimental interest in Fe- and Co-containing compounds was 2-fold: (i) to achieve future targeted property modifications by fine-tuning the Fermi level position via aliovalent substitution, the synthesis of corresponding parent ternary phases needs to be developed; (ii) such boron-rich layered structures with boron networks analogous to MgB_2 call for experimental verification of the presence or absence of superconductivity in those compounds. We focused on the synthesis of YFeB_4 and YCoB_4 . While the formation of YCoB_4 was observed in the experimental samples as one of the major phases, we were not able to reduce the amounts of admixtures to a minimum level, and the properties of YCoB_4 were not investigated.

Arc-melting of the stoichiometric YFeB_4 samples resulted in ingots containing a mixture of two major phases, YFeB_4 and YB_4 , along with minor impurities of Y_2O_3 and YFe_2B_2 . Single crystals of YFeB_4 were obtained, and the crystal structure was refined using single-crystal X-ray diffraction. Synthetic efforts were undertaken to characterize YFeB_4 properties, aiming at a

single-phase sample of YFeB_4 . To suppress the formation of the YB_4 phase, an excess of Fe was loaded into the starting composition (Figure 6). As expected, the excess of Fe reduced

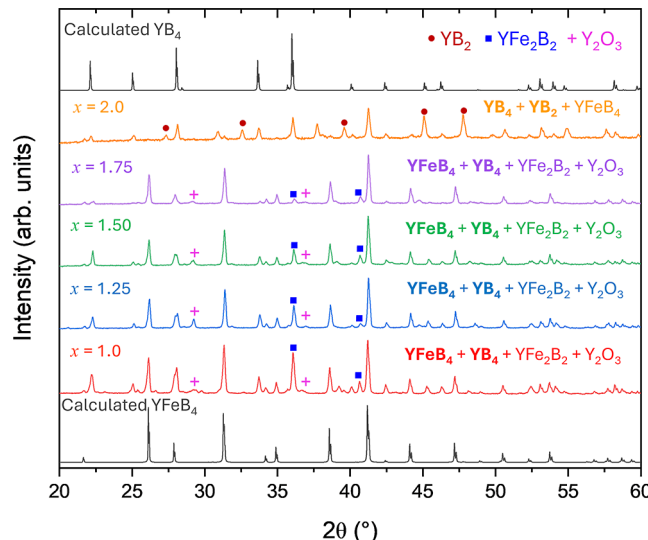


Figure 6. Experimental powder X-ray diffraction (PXRD) patterns (colored) of the arc-melted ingots with varying loaded compositions of $1\text{Y} + x\text{Fe} + 4\text{B}$, where $x = 1.0, 1.25, 1.5, 1.75$, and 2.0 . The values of x are indicated on the top left corner of the PXRD pattern. The calculated patterns of YFeB_4 (based on the single-crystal structural model) and YB_4 are shown in black on the bottom and top, respectively. The phase composition for each sample as determined by PXRD is provided above each pattern with the major phase(s) indicated in bold text. The most intense peaks of Y_2O_3 (+, pink cross), YFe_2B_2 (■, blue squares), and YB_2 (●, red circles) are also indicated.

the formation of YB_4 but resulted in an incomplete elimination of the admixture. Moreover, samples with $>25\%$ of Fe excess exhibited an increase in the formation of YFe_2B_2 impurity.

Further treatment was applied to reduce the impurity phases. Heat treatment of the arc-melted ingots for 120 h at 1050 °C in evacuated sealed silica ampules was used to improve the homogeneity of the sample. This allowed for YB_4 and Fe-containing admixture phases to react further and yield YFeB_4 (Figure 7). Finally, an acid wash in 3 M HCl was used to remove some of the remaining impurities, because the target YFeB_4 phase is stable under these acid washing conditions.

Thus, the optimized synthesis of YFeB_4 required the arc-melting of samples containing a Fe excess, 25–50 at. %. After arc-melting, the samples were isothermally annealed at 1050 °C for 120 h, followed by HCl acid-washing the finely ground polycrystalline samples overnight (see Figure 7). This optimized synthesis yields YFeB_4 samples with minimal impurities, suitable for basic property characterization. Characterization of the basic properties for YFeB_4 is presented in Texts S1 and S2 of the Supporting Information.

Single-Crystal Diffraction. The crystal structure of YCrB_4 was recently redetermined with the single-crystal diffraction method.⁷⁰ In general, in the structures of borides, mixed occupancy and vacancies in metal sites may occur, which can, in turn, affect the position of the Fermi level and result in properties that are different from the expected properties for stoichiometric compounds. We determined the crystal structure of YFeB_4 . The refinement of the single-crystal diffraction data reveals 100% occupancy of Fe and Y sites

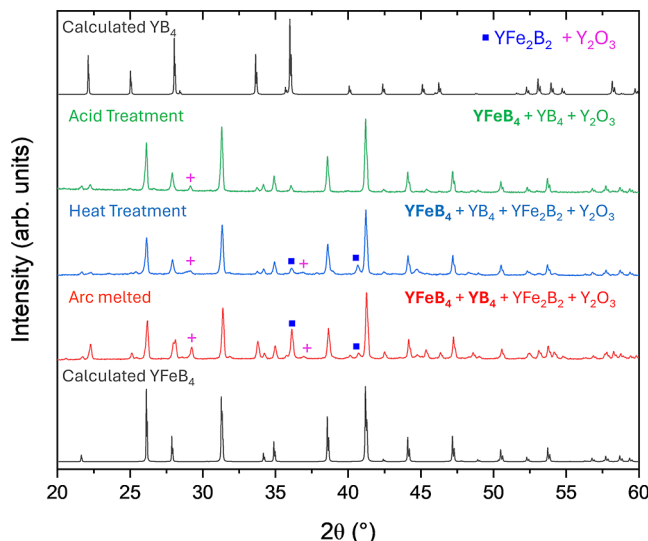


Figure 7. PXRD patterns of the sample with a loaded composition of $\text{Y} + 1.5\text{Fe} + 4\text{B}$. The sample was arc-melted (red pattern) and then annealed isothermally at 1050°C for 5 days (blue pattern), followed by being ground into a fine powder and acid-washed using 3 M HCl (green pattern). Theoretical powder patterns of YB_4 and YFeB_4 (both black) are shown on the top and bottom, respectively. The most intense peaks of Y_2O_3 (+, pink cross) and YFe_2B_2 (■, blue squares) are indicated along with the phase composition for each sample. Bold text indicates a major phase.

with no Y/Fe mixing or vacancies. In the structure of YFeB_4 determined at 100 K, the B–B distances vary in the 1.689(9)–1.825(7) Å range. This is comparable to the range of B–B distances in YCrB_4 determined at 294 K: 1.72–1.83 Å. Replacing Cr with Fe resulted in a significant increase in the metal–metal distance in the dimer from 2.374 Å for Cr–Cr to 2.539(1) Å for Fe–Fe. The latter distance agrees with the computationally predicted Fe–Fe distance (2.546 Å, $\Delta = 0.28\%$) for the optimized structure. Further details of the crystal structure are provided in Table 3 and in the CCDC deposition number 2325813.

Comparison with a Related Fe Substructure and Discussion. A pioneer work on the similar Fe-ladder formation in borides is the study of $\text{Ti}_9\text{Fe}_2\text{Ru}_{18}\text{B}_8$.⁷¹ Similar to the Fe ladders in YFeB_4 , in $\text{Ti}_9\text{Fe}_2\text{Ru}_{18}\text{B}_8$, the intradimer distance is the shortest (~2.5 Å), followed by interdimer distance along the ladder (~3 Å), and the interladder distance is the longest (~11 Å). The intradimer distance in YFeB_4 (2.539 Å) is very similar to that in $\text{Ti}_9\text{Fe}_2\text{Ru}_{18}\text{B}_8$, while the interdimer distance in YFeB_4 (3.409 Å) is longer. Therefore, the dimers in YFeB_4 are more isolated along the ladder, and the interdimer coupling is weaker. The interdimer coupling in $\text{Ti}_9\text{Fe}_2\text{Ru}_{18}\text{B}_8$ is stronger, and a “ladder” picture suits it better. $\text{Ti}_9\text{Fe}_2\text{Ru}_{18}\text{B}_8$ orders ferromagnetically between 10 and 200 K,⁷¹ for which the Fe ladders play a crucial role. Its ferromagnetism is found to be caused by the FM coupling among neighboring spin-triplet Fe_2 dimers along the ladder.⁷¹ Also, a local maximum in the NM DOS at the Fermi level leads $\text{Ti}_9\text{Fe}_2\text{Ru}_{18}\text{B}_8$ to ferromagnetism.^{71,72} In contrast, the two VHS formed by the Fe dimer in YFeB_4 lie below the Fermi level, and the Fermi level is at a local minimum of DOS. The low DOS is not sufficient to satisfy the Stoner criterion and generate ferromagnetism. YFeB_4 is thereby predicted to be NM.

Further substitution of Ti by Fe in $\text{Ti}_9\text{Fe}_2\text{Ru}_{18}\text{B}_8$, i.e., $\text{Ti}_{9-x}\text{Fe}_{2+x}\text{Ru}_{18}\text{B}_8$, forms additional Fe chains.^{72,73} An Fe ladder

Table 3. Data Collection and Structure Refinement Parameters for YFeB_4 ^a

compound	YFeB_4
CSD-numbers	2325813
temperature (K)	100
radiation (Å)	$\text{Mo}-K_{\alpha}$ 0.71037
crystal system	orthorhombic
space group	$Pbam$ (no. 55)
a [Å]	5.9049(3)
b [Å]	11.4160(6)
c [Å]	3.4094(2)
volume [Å ³]	229.83(2)
Z	4
data/parameters	533/37
density (g/cm ³)	5.43
u (mm ⁻¹)	31.01
R_{int}	0.043
GOF	1.38
R_1 [$I > 2\sigma(I)$]	0.028
wR_2 [$I > 2\sigma(I)$]	0.078
R_1	0.030
wR_2	0.080
diff. peaks [e Å ⁻³]	1.34/−1.31

^aThe deposition number 2325813 contains supplementary crystallographic data. These data are provided free of charge by the joint Cambridge Crystallographic Data Centre and FIZ Karlsruhe Access Structures service (<https://www.ccdc.cam.ac.uk/structures>).

and two Fe chains next to the Fe ladder form an Fe scaffold.^{72,73} The interplay between magnetically active structures and magnetic states is seen in this series of compounds. With increasing Fe content, phase transitions from FM to different ferrimagnetic states, accompanied by unexpected magnetic moment decrease and then increase, were observed.^{72,73} These related studies provide valuable insights into future studies on aliovalent substitution in YFeB_4 and other MTB₄ systems. Different substitution possibilities include (i) magnetically active or inactive elements; (ii) M or T site; or (iii) mixed dimer, mixed ladder, or mixed lattice.

CONCLUSIONS

In summary, using first-principles calculations, we identified 21 structurally stable and 25 metastable ternary metal borides of MTB₄-type (M = Sc, Y, La, Ce, Lu, Mg, Ca, and Al; T = V, Cr, Mn, Fe, Co, and Ni). Among them, we uncovered 20 magnetic systems, the rest being NM. Electronic and magnetic calculations for this family of materials reveal similarities in their electronic and magnetic structures for those compounds with the same valence shell electron count. Magnetism in these compounds is dominated by strong AFM Cr (both Cr and Mn for M = Mg and Ca) or FM Mn (Fe instead for M = Mg and Ca) interactions within the structural dimers with much weaker interactions between the dimers. The magnetic ground states in DFT are semiconducting or weakly metallic for these systems. Mn compounds are predicted to be conventional Néel antiferromagnets with layered (A-type) ordering and T_N below room temperature. In contrast, Cr compounds are proposed to be close to a QCP between a singlet spin-dimer phase, with a spin gap above room temperature, and the conventional Néel AFM phase. In total, we unveiled 9 dimerized quantum spin-gap systems and 11 conventional antiferromagnets. Four of the dimerized quantum magnets are stable (ScCrB_4 , YCrB_4 ,

LuCrB_4 , and MgMnB_4) and 5 are metastable (MgCrB_4 , CaCrB_4 , AlCrB_4 , LaCrB_4 , and CaMnB_4). They provide a unique possibility for investigating BEC of magnetic excitations in crystalline systems.² The prediction of this new family of dimerized quantum magnets greatly expands the materials inventory that allows such an investigation.² Six of the conventional antiferromagnets are stable (CeCrB_4 , ScMnB_4 , YMnB_4 , CeMnB_4 , LuMnB_4 , and MgFeB_4) and 5 are metastable (AlMnB_4 , LaMnB_4 , CaFeB_4 , LaFeB_4 , and CeFeB_4). Experimental methods to produce YFeB_4 crystals for structural analysis and samples suitable for characterization are reported. The similarities and differences of the Fe dimers and Fe ladders in YFeB_4 compared to related structures in previous studies are discussed. All the stable and metastable MTB_4 systems identified in this study, whether quantum magnetic, conventional magnetic, or NM, provide a platform with numerous possibilities for future doping on the M site or the T site. Tuning the magnetic exchange coupling by doping may facilitate the study of this rare type of quantum phase transition across the spin-gap QCP. This work offers new opportunities for studying the quantum magnetism of spin dimers in borides. The step-by-step methodology used in this work also demonstrates a theoretical workflow for future searches for dimerized quantum magnets in other families or types of materials.

METHODS

DFT Calculations. We conducted DFT calculations using the projector augmented wave method⁷⁴ as implemented in the VASP package.⁷⁵ The exchange–correlation energy was treated by the Perdew–Burke–Ernzerhof⁷⁶ GGA. A plane-wave-basis set was used with a kinetic energy cutoff of 520 eV. The convergence thresholds were 10^{-5} eV for electronic self-consistency and $0.01 \text{ eV } \text{\AA}^{-1}$ for ionic relaxation. The tetrahedron method with Blöchl corrections was used for the Brillouin zone integration. In the structural optimization, the Brillouin zone was sampled by the Monkhorst–Pack scheme with a *k*-point grid of $2\pi \times 0.033 \text{ \AA}^{-1}$. In the static calculations, energy, magnetic moments, and electronic DOS were computed with a denser *k*-point grid of $2\pi \times 0.022 \text{ \AA}^{-1}$.

Real-Space Paramagnetic Pauli Spin Susceptibility Matrix Calculations. Electronic instabilities suggest that analysis of the possibility of local magnetic moments and magnetic order stabilization is required. Take Y compounds, for example. As discussed in the main text, Fe, Co, and Ni compounds are good metals, but according to the Stoner criterion, their $N(E_f)$ is insufficient to generate FM instability. In contrast, in YMnB_4 , the Fermi level is located at a peak with $N(E_f) > 1 \text{ eV}^{-1} \text{ f.u.}^{-1} \text{ spin}^{-1}$. Thus, ferromagnetism in Mn compounds is plausible, while the insulating state of Cr compounds suggests antiferromagnetism as the most likely option. Accordingly, we calculated the real-space paramagnetic Pauli spin susceptibility matrix (see details in ref⁷⁷) for transition-metal atoms and their neighbors. As expected, the important elements of χ_{ij} involve transition-metal atoms and their dimer partners. The on-site term χ_{00} dominates, and the intradimer matrix element χ_{ij} is about 10% of the former in magnitude. The Anderson local moment criterion ($S_{00} = I\chi_{00} > 1$) is barely satisfied in Mn ($S_{00} = 1.08$), marginal in Cr ($S_{00} = 0.98$), and not satisfied in all other YTB_4 systems. However, the generalization of the Anderson local moment criterion is satisfied for a FM dimer in YMnB_4 with $I(\chi_{00} + \chi_{01}) = 1.2$ and for an AFM dimer in YCrB_4 with $I(\chi_{00} - \chi_{01}) = 1.1$. For all other YTB_4 systems, local moments on a single dimer are unstable. Thus, while the local magnetic instability on Cr and Mn atoms is likely, the resulting atomic moment can be classified as weakly local. This can be compared to strong local moment systems such as bcc iron, where $S_{00} = 1.6$.⁷⁷ The values obtained above are somewhat similar to the situation in hcp cobalt.⁷⁷ However, calculations of susceptibility in cases of weak local moments may not be reliable, and only more

precise full-potential self-consistent calculations of the magnetic ground state as seen in the main text can provide a justified answer.

Synthesis. High-purity Y fingers (99.9999%) were acquired from the Materials Preparation Center at Ames National Laboratory. Other chemicals were received from Alfa Aesar: Fe powder (99.9%), Co powder (99.5%), and amorphous B powder (98%). Y fingers were cut into small pieces and weighed out to approximately 230 mg. Based on Y weight and desired molar ratio, i.e., 1:1:4 or 1:1.5:4, Fe and amorphous B amounts were recalculated and weighed out. The mixture of Fe and B was then cold-pressed into a pellet. The total sample weight (Y + Fe + B) was approximately 500 mg. Yttrium pieces and the (Fe + 4B) pellet were placed onto a water-cooled copper hearth in a tungsten anode arc melter. The chamber was evacuated for 20 min and filled with Ar gas. Additionally, a Zr getter was placed in the chamber and arced to remove any traces of oxygen. The YFeB_4 sample was arc-melted, and then the ingot was flipped and remelted. This process was repeated four times. A similar procedure was applied for Co-containing samples.

Annealing. After arc melting, selected samples were loaded into a carbonized silica ampule, which was evacuated and flamed sealed. The ampules were placed into a muffle furnace and heated to 1050 °C with a heating rate of 175 °C per hour. Once at 1050 °C, the samples were isothermally annealed for 120 h. The furnace was turned off and allowed to cool. After annealing, the ingot sample was ground into a fine powder using a tungsten carbide mortar in air.

Selected annealed samples were acid-washed to reduce impurities. Our studies indicated that the target YFeB_4 phase is acid-stable. The samples were washed in 3 M hydrochloric acid overnight to remove YB_4 and any Fe impurities. After that, the sample was filtered, washed with distilled water, and dried in air.

Powder X-ray Diffraction. The samples were characterized using PXRD on a Rigaku MiniFlex 600 powder diffractometer with $\text{Cu}-K_a$ radiation ($\lambda = 1.54059 \text{ \AA}$) and a $\text{Ni}-K_b$ filter. Fluorescence reduction was used to minimize background fluorescence from Fe.

Single-Crystal X-ray Diffraction. Single crystals of YFeB_4 were picked out from a crushed ingot with a loaded composition of Y + Fe + 4B. No further treatment was done to the ingot after arc melting. The single-crystal diffraction experiment was conducted using a Bruker D8 Venture diffractometer with a PHOTON detector and $\text{Mo}-K_a$ radiation. The crystal was cooled to 100 K with a stream of nitrogen gas. Structure determination and the final refinement of the data set were carried out using the SHELX suite of programs. Refining of the occupancies of Fe and Y indicated no deviations from 100% within one standard uncertainty.

Scanning Electron Microscopy and Energy Dispersion X-ray Spectroscopy. Elemental analysis was carried out using an FEI Quanta 250 field emission scanning electron microscope with an energy dispersion X-ray spectroscopy (EDS) detector (Oxford X-Max 80, Thermo Fischer Scientific, Inc.). The resulting data were analyzed using the Aztec software. Powdered samples were mounted in epoxy, polished to a level surface, and coated with a conductive layer of carbon. An accelerating voltage of 15 kV was used. Compositions were normalized with respect to 1 Y atom to provide information about the Y/Fe ratio. The quantification of light elements, such as B, is not accurate using this technique, but the presence of B was evident from EDS spectra and elemental mapping (see Figure S6 of the Supporting Information).

Magnetic Measurements. Magnetic properties were measured by an MPMS-XL SQUID magnetometer (Quantum Design) on two polycrystalline YFeB_4 samples. The temperature dependence of the magnetic susceptibility was measured from 2 to 300 K at applied magnetic fields of 0.1 and 2 T. The isothermal magnetization field dependence was measured from −7 to 7 T at 2 and 300 K.

Resistivity Measurements. A physical property measurement system (PPMS, Quantum Design) was used to characterize the electrical resistivity of the arc-melted ingot of YFeB_4 (see Figure S7 of the Supporting Information). The ingot was sanded down until a smooth flat surface remained. A 50 mm platinum wire was attached to the smooth surface using conductive silver paste. A four-probe method was used for the measurements.

Heat Capacity Measurements. Heat capacity was measured from 3.5 to 300 K using the heat capacity option of the Quantum Design PPMS. The small part of the ingot (13.4 mg) was mounted to the sample platform with Apiezon "N" grease. An addendum measurement containing the heat capacity of the grease was subtracted from the total heat capacity.

■ ASSOCIATED CONTENT

SI Supporting Information

The Supporting Information is available free of charge at <https://pubs.acs.org/doi/10.1021/jacs.4c05478>.

Computationally predicted β -phase stabilities, distances between the transition-metal atoms, basic property characterization, electron–phonon coupling strength, and SEM EDS analysis of YFeB₄ ([PDF](#))

Accession Codes

CCDC 2325813 contains the supplementary crystallographic data for this paper. These data can be obtained free of charge via www.ccdc.cam.ac.uk/data_request/cif or by emailing data_request@ccdc.cam.ac.uk or by contacting The Cambridge Crystallographic Data Centre, 12 Union Road, Cambridge CB2 1EZ, UK; fax: +44 1223 336033.

■ AUTHOR INFORMATION

Corresponding Authors

Yang Sun — Department of Physics, Xiamen University, Xiamen 361005, China;  orcid.org/0000-0002-4344-2920; Email: yangsun@xmu.edu.cn

Kirill D. Belashchenko — Department of Physics and Astronomy and Nebraska Center for Materials and Nanoscience, University of Nebraska-Lincoln, Lincoln, Nebraska 68588, United States; Email: belashchenko@unl.edu

Kirill Kovnir — Department of Chemistry, Iowa State University, Ames, Iowa 50011, United States; Ames National Laboratory, U.S. Department of Energy, Ames, Iowa 50011, United States;  orcid.org/0000-0003-1152-1912; Email: kovnir@iastate.edu

Vladimir Antropov — Department of Physics and Astronomy, Iowa State University, Ames, Iowa 50011, United States; Ames National Laboratory, U.S. Department of Energy, Ames, Iowa 50011, United States; Email: antropov@iastate.edu

Authors

Zhen Zhang — Department of Physics and Astronomy, Iowa State University, Ames, Iowa 50011, United States;  orcid.org/0009-0001-0810-8054

Andrew P. Porter — Department of Chemistry, Iowa State University, Ames, Iowa 50011, United States; Ames National Laboratory, U.S. Department of Energy, Ames, Iowa 50011, United States

Gayatri Viswanathan — Department of Chemistry, Iowa State University, Ames, Iowa 50011, United States; Ames National Laboratory, U.S. Department of Energy, Ames, Iowa 50011, United States

Arka Sarkar — Department of Chemistry, Iowa State University, Ames, Iowa 50011, United States; Ames National Laboratory, U.S. Department of Energy, Ames, Iowa 50011, United States

Eranga H. Gamage — Department of Chemistry, Iowa State University, Ames, Iowa 50011, United States; Ames National

Laboratory, U.S. Department of Energy, Ames, Iowa 50011, United States;  orcid.org/0000-0002-6954-7130

Kai-Ming Ho — Department of Physics and Astronomy, Iowa State University, Ames, Iowa 50011, United States

Complete contact information is available at:
<https://pubs.acs.org/10.1021/jacs.4c05478>

Author Contributions

#Z.Z. and A.P.P. contributed equally.

Notes

The authors declare no competing financial interest.

■ ACKNOWLEDGMENTS

We would like to thank Dr. Sergey Bud'ko (Ames National Laboratory) for the useful discussions and Dr. Yaroslav Mudryk (Ames National Laboratory) for the magnetic measurements. This work is supported by the U.S. Department of Energy (DOE) Established Program to Stimulate Competitive Research (EPSCoR) grant no. DE-SC0024284. Computations were performed at the High Performance Computing facility at Iowa State University and the Holland Computing Center at the University of Nebraska. The PPMS instrument used for property measurements was supported by Ames National Laboratory, U.S. Department of Energy, which operates under the contract DE-AC02-07CH11358. Y.S. acknowledges support by the Natural Science Foundation of Xiamen (grant no. 3502Z202371007), the Fundamental Research Funds for the Central Universities (grant no. 20720230014), and the National Natural Science Foundation of China (NSFC) (grant no. 42374108).

■ REFERENCES

- (1) Balents, L. Spin Liquids in Frustrated Magnets. *Nature* **2010**, *464*, 199–208.
- (2) Zapf, V.; Jaime, M.; Batista, C. D. Bose–Einstein condensation in quantum magnets. *Rev. Mod. Phys.* **2014**, *86*, 563–614.
- (3) Matsumoto, M.; Normand, B.; Rice, T. M.; Sigrist, M. Field- and pressure-induced magnetic quantum phase transitions in TlCuCl₃. *Phys. Rev. B: Condens. Matter Mater. Phys.* **2004**, *69*, 054423.
- (4) Sebastian, S. E.; Harrison, N.; Batista, C. D.; Balicas, L.; Jaime, M.; Sharma, P. A.; Kawashima, N.; Fisher, I. R. Dimensional reduction at a quantum critical point. *Nature* **2006**, *441*, 617–620.
- (5) Nikuni, T.; Oshikawa, M.; Oosawa, A.; Tanaka, H. Bose–Einstein condensation of dilute magnons in TlCuCl₃. *Phys. Rev. Lett.* **2000**, *84*, 5868–5871.
- (6) Kodama, K.; Takigawa, M.; Horvatić, M.; Berthier, C.; Kageyama, H.; Ueda, Y.; Miyahara, S.; Becca, F.; Mila, F. Magnetic superstructure in the two-dimensional quantum antiferromagnet SrCu₂(BO₃)₂. *Science* **2002**, *298*, 395–399.
- (7) Rüegg, C.; Cavaldini, N.; Furrer, A.; Güdel, H. U.; Krämer, K.; Mutka, H.; Wildes, A.; Habicht, K.; Vorderwisch, P. Bose–Einstein condensation of the triplet states in the magnetic insulator TlCuCl₃. *Nature* **2003**, *423*, 62–65.
- (8) Jaime, M.; Correa, V. F.; Harrison, N.; Batista, C. D.; Kawashima, N.; Kazuma, Y.; Jorge, G. A.; Stern, R.; Heinmaa, I.; Zvyagin, S. A.; Sasago, Y.; Uchinokura, K. Magnetic-field-induced condensation of triplons in Han Purple pigment BaCuSi₂O₆. *Phys. Rev. Lett.* **2004**, *93*, 087203.
- (9) Rüegg, C.; McMorrow, D. F.; Normand, B.; Rønnow, H. M.; Sebastian, S. E.; Fisher, I. R.; Batista, C. D.; Gvasaliya, S. N.; Niedermayer, C.; Stahn, J. Multiple magnon modes and consequences for the Bose–Einstein condensed phase in BaCuSi₂O₆. *Phys. Rev. Lett.* **2007**, *98*, 017202.
- (10) Sengupta, P.; Batista, C. D. Field-induced supersolid phase in spin-one Heisenberg models. *Phys. Rev. Lett.* **2007**, *98*, 227201.

- (11) Stone, M. B.; Lumsden, M. D.; Chang, S.; Samulon, E. C.; Batista, C. D.; Fisher, I. R. Singlet-triplet dispersion reveals additional frustration in the triangular-lattice dimer compound $\text{Ba}_3\text{Mn}_2\text{O}_8$. *Phys. Rev. Lett.* **2008**, *100*, 237201.
- (12) Samulon, E. C.; Jo, Y. J.; Sengupta, P.; Batista, C. D.; Jaime, M.; Balicas, L.; Fisher, I. R. Ordered magnetic phases of the frustrated spin-dimer compound $\text{Ba}_3\text{Mn}_2\text{O}_8$. *Phys. Rev. B: Condens. Matter Mater. Phys.* **2008**, *77*, 214441.
- (13) Samulon, E. C.; Kohama, Y.; McDonald, R. D.; Shapiro, M. C.; Al-Hassanieh, K. A.; Batista, C. D.; Jaime, M.; Fisher, I. R. Asymmetric quintuplet condensation in the frustrated $S = 1$ spin dimer compound $\text{Ba}_3\text{Mn}_2\text{O}_8$. *Phys. Rev. Lett.* **2009**, *103*, 047202.
- (14) Oosawa, A.; Fujisawa, M.; Osakabe, T.; Kakurai, K.; Tanaka, H. Neutron diffraction study of the pressure-induced magnetic ordering in the spin gap system TlCuCl_3 . *J. Phys. Soc. Jpn.* **2003**, *72*, 1026–1029.
- (15) Tanaka, H.; Goto, K.; Fujisawa, M.; Ono, T.; Uwatoko, Y. Magnetic ordering under high pressure in the quantum spin system TlCuCl_3 . *Phys. B* **2003**, *329–333*, 697–698.
- (16) Rüegg, C.; Furrer, A.; Sheptyakov, D.; Strässle, T.; Krämer, K. W.; Güdel, H. U.; Mélési, L. Pressure-induced quantum phase transition in the spin-liquid TlCuCl_3 . *Phys. Rev. Lett.* **2004**, *93*, 257201.
- (17) Rüegg, C.; Normand, B.; Matsumoto, M.; Furrer, A.; McMorrow, D. F.; Krämer, K. W.; Güdel, H. U.; Gvasaliya, S. N.; Mutka, H.; Boehm, M. Quantum magnets under pressure: controlling elementary excitations in TlCuCl_3 . *Phys. Rev. Lett.* **2008**, *100*, 205701.
- (18) Merchant, P.; Normand, B.; Krämer, K. W.; Boehm, M.; McMorrow, D. F.; Rüegg, C. Quantum and classical criticality in a dimerized quantum antiferromagnet. *Nat. Phys.* **2014**, *10*, 373–379.
- (19) Oosawa, A.; Ono, T.; Tanaka, H. Impurity-induced antiferromagnetic ordering in the spin gap system TlCuCl_3 . *Phys. Rev. B: Condens. Matter Mater. Phys.* **2002**, *66*, 020405.
- (20) Manna, S.; Majumder, S.; De, S. K. Tuning of the spin gap transition of spin dimer compound $\text{Ba}_3\text{Mn}_2\text{O}_8$ by doping with La and V. *J. Phys.: Condens. Matter* **2009**, *21*, 236005.
- (21) Rice, T. M. To condense or not to condense. *Science* **2002**, *298*, 760–761.
- (22) Sasago, Y.; Uchinokura, K.; Zheludev, A.; Shirane, G. Temperature-dependent spin gap and singlet ground state in $\text{BaCuSi}_2\text{O}_6$. *Phys. Rev. B: Condens. Matter Mater. Phys.* **1997**, *55*, 8357–8360.
- (23) Uchida, M.; Tanaka, H.; Mitamura, H.; Ishikawa, F.; Goto, T. High-field magnetization process in the $S=1$ quantum spin system $\text{Ba}_3\text{Mn}_2\text{O}_8$. *Phys. Rev. B: Condens. Matter Mater. Phys.* **2002**, *66*, 054429.
- (24) Matkovich, V. I., Ed.; *Boron and Refractory Borides*; Springer: Berlin, 1977.
- (25) Scheifers, J. P.; Zhang, Y.; Fokwa, B. P. T. Boron: Enabling exciting metal-rich structures and magnetic properties. *Acc. Chem. Res.* **2017**, *50*, 2317–2325.
- (26) Akopov, G.; Yeung, M. T.; Kaner, R. B. Rediscovering the crystal chemistry of borides. *Adv. Mater.* **2017**, *29*, 1604506.
- (27) Zhang, S.; Wang, Q.; Kawazoe, Y.; Jena, P. Three-dimensional metallic boron nitride. *J. Am. Chem. Soc.* **2013**, *135*, 18216–18221.
- (28) Mbarki, M.; St Touzani, R.; Fokwa, B. P. T. Unexpected synergy between magnetic iron chains and stacked B_6 rings in $\text{Nb}_6\text{Fe}_{1-x}\text{Ir}_{6+x}\text{B}_8$. *Angew. Chem.* **2014**, *126*, 13390–13393.
- (29) Shankhari, P.; Bakshi, N. G.; Zhang, Y.; Stekovic, D.; Itkis, M. E.; Fokwa, B. P. T. A delicate balance between antiferromagnetism and ferromagnetism: Theoretical and experimental studies of $\text{A}_2\text{MRu}_3\text{B}_2$ ($\text{A} = \text{Zr}, \text{Hf}$; $\text{M} = \text{Fe}, \text{Mn}$) metal borides. *Chem.—Eur. J.* **2020**, *26*, 1979–1988.
- (30) Sharma, N.; Zhang, Y.; Mbarki, M.; Scheifers, J. P.; Yubuta, K.; Kimber, S. A. J.; Fokwa, B. P. T. $\text{Nb}_6\text{Mn}_{1-x}\text{Ir}_{6+x}\text{B}_8$ ($x = 0.25$): A ferrimagnetic boride containing planar B_6 rings interacting with ferromagnetic Mn chains. *J. Phys. Chem. C* **2021**, *125*, 13635–13640.
- (31) Scheifers, J. P.; Flores, J. H.; Janka, O.; Pöttgen, R.; Fokwa, B. P. T. Triangular arrangement of ferromagnetic iron chains in the high- T_{C} ferromagnet $\text{TiFe}_{1-x}\text{Os}_{2+x}\text{B}_2$. *Chem.—Eur. J.* **2022**, *28*, No. e202201058.
- (32) Park, H.; Encinas, A.; Scheifers, J. P.; Zhang, Y.; Fokwa, B. P. T. Boron-dependency of molybdenum boride electrocatalysts for the hydrogen evolution reaction. *Angew. Chem., Int. Ed.* **2017**, *56*, 5575–5578.
- (33) Jothi, P. R.; Zhang, Y.; Yubuta, K.; Culver, D. B.; Conley, M.; Fokwa, B. P. T. Abundant vanadium diboride with graphene-like boron layers for hydrogen evolution. *ACS Appl. Energy Mater.* **2019**, *2*, 176–181.
- (34) Woo, K. E.; Kong, S.; Chen, W.; Chang, T. H.; Viswanathan, G.; Díez, A. M.; Sousa, V.; Kolen'ko, Y. V.; Lebedev, O. I.; Costa Figueiredo, M.; Kovnir, K. Topotactic BI_3 -assisted borodization: synthesis and electrocatalysis applications of transition metal borides. *J. Mater. Chem. A* **2022**, *10*, 21738–21749.
- (35) Saglik, K.; Mete, B.; Terzi, I.; Candolfi, C.; Aydemir, U. Thermoelectric borides: Review and future perspectives. *Adv. Phys. Res.* **2023**, *2*, 2300010.
- (36) Yeung, M. T.; Mohammadi, R.; Kaner, R. B. Ultra-incompressible, superhard materials. *Annu. Rev. Mater. Res.* **2016**, *46*, 465–485.
- (37) Akopov, G.; Roh, I.; Sobell, Z. C.; Yeung, M. T.; Pangilinan, L.; Turner, C. L.; Kaner, R. B. Effects of variable boron concentration on the properties of superhard tungsten tetraboride. *J. Am. Chem. Soc.* **2017**, *139*, 17120–17127.
- (38) Akopov, G.; Yeung, M. T.; Roh, I.; Sobell, Z. C.; Yin, H.; Mak, W. H.; Khan, S. I.; Kaner, R. B. Effects of dodecaboride-forming metals on the properties of superhard tungsten tetraboride. *Chem. Mater.* **2018**, *30*, 3559–3570.
- (39) Akopov, G.; Yeung, M. T.; Sobell, Z. C.; Turner, C. L.; Lin, C. W.; Kaner, R. B. Superhard mixed transition metal dodecaborides. *Chem. Mater.* **2016**, *28*, 6605–6612.
- (40) Nagamatsu, J.; Nakagawa, N.; Muranaka, T.; Zenitani, Y.; Akimitsu, J. Superconductivity at 39 K in magnesium diboride. *Nature* **2001**, *410*, 63–64.
- (41) Kortus, J.; Mazin, I. I.; Belashchenko, K. D.; Antropov, V. P.; Boyer, L. L. Superconductivity of metallic boron in MgB_2 . *Phys. Rev. Lett.* **2001**, *86*, 4656–4659.
- (42) An, J. M.; Pickett, W. E. Superconductivity of MgB_2 : Covalent bonds driven metallic. *Phys. Rev. Lett.* **2001**, *86*, 4366–4369.
- (43) Liu, A. Y.; Mazin, I. I.; Kortus, J. Beyond Eliashberg superconductivity in MgB_2 : Anharmonicity, two-phonon scattering, and multiple gaps. *Phys. Rev. Lett.* **2001**, *87*, 087005.
- (44) Gutfleisch, O.; Willard, M. A.; Brück, E.; Chen, C. H.; Sankar, S. G.; Liu, J. P. Magnetic materials and devices for the 21st century: Stronger, lighter, and more energy efficient. *Adv. Mater.* **2011**, *23*, 821–842.
- (45) Simonson, J. W.; Poon, S. J. Applying an electron counting rule to screen prospective thermoelectric alloys: The thermoelectric properties of YCrB_4 and Er_3CrB_7 -type phases. *J. Alloys Compd.* **2010**, *504*, 265–272.
- (46) Flipo, S.; Rosner, H.; Bobnar, M.; Kvashnina, K. O.; Leithe-Jasper, A.; Gumeniuk, R. Thermoelectricity and electronic properties of $\text{Y}_{1-x}\text{Ce}_x\text{CrB}_4$. *Phys. Rev. B* **2021**, *103*, 195121.
- (47) Candan, A.; Surucu, G.; Gencer, A. Electronic, mechanical and lattice dynamical properties of YXB_4 ($\text{X} = \text{Cr}, \text{Mn}, \text{Fe}$, and Co) compounds. *Phys. Scr.* **2019**, *94*, 125710.
- (48) Akopov, G.; Pangilinan, L. E.; Mohammadi, R.; Kaner, R. B. Perspective: Superhard metal borides: A look forward. *APL Mater.* **2018**, *6*, 70901.
- (49) Akopov, G.; Yin, H.; Roh, I.; Pangilinan, L. E.; Kaner, R. B. Investigation of hardness of ternary borides of the YCrB_4 , Y_2ReB_6 , Y_3ReB_7 , and YMo_3B_7 structural types. *Chem. Mater.* **2018**, *30*, 6494–6502.
- (50) Kuzma, Y. B. Crystal structure of the compound YCrB_4 and its analogs. *Sov. Phys. Crystallogr.* **1970**, *15*, 372–374.
- (51) Kuzma, Y. B. New ternary compounds with the structure of YCrB_4 type. *Dopov. Akad. Nauk Ukr. RSR, Ser. A: Fiz.-Mat. Tekh. Nauki* **1970**, *8*, 756–758.

- (52) Rogl, P. Borides with Two-Dimensional Boron Networks. *Inorg. React. Methods* **1991**, *13*, 156–167.
- (53) Rogl, P. Chapter 49 Phase equilibria in ternary and higher order systems with rare earth elements and boron. *Handbook on the Physics and Chemistry of Rare Earths*; Elsevier, 1984; Vol. 6; pp 335–523.
- (54) Rogl, P. New ternary borides with YCrB_4 -type structure. *Mater. Res. Bull.* **1978**, *13*, 519–523.
- (55) Medvedeva, N. I.; Medvedeva, Y. E.; Ivanovskii, A. L. Electronic structure of ternary boron-containing phases YCrB_4 , Y_2ReB_6 , and MgC_2B_2 . *Dokl. Phys. Chem.* **2002**, *383*, 75–77.
- (56) Sun, Y.; Zhang, Z.; Porter, A. P.; Kovnir, K.; Ho, K. M.; Antropov, V. Prediction of Van Hove singularity systems in ternary borides. *npj Comput. Mater.* **2023**, *9*, 204.
- (57) Prasad, A.; Hossain, Z.; Jeevan, H. S.; Geibel, C. YbNiB_4 : A Kondo Lattice with Low-Dimensional Antiferromagnetic Fluctuations. *J. Phys.: Condens. Matter* **2009**, *21*, 206003.
- (58) Jain, A.; Ong, S. P.; Hautier, G.; Chen, W.; Richards, W. D.; Dacek, S.; Cholia, S.; Gunter, D.; Skinner, D.; Ceder, G.; Persson, K. A. Commentary: The materials project: A materials genome approach to accelerating materials innovation. *APL Mater.* **2013**, *1*, 011002.
- (59) Kirklin, S.; Saal, J. E.; Meredig, B.; Thompson, A.; Doak, J. W.; Aykol, M.; Rühl, S.; Wolverton, C. The Open Quantum Materials Database (OQMD): assessing the accuracy of DFT formation energies. *npj Comput. Mater.* **2015**, *1*, 15010.
- (60) Sun, W.; Dacek, S. T.; Ong, S. P.; Hautier, G.; Jain, A.; Richards, W. D.; Gamst, A. C.; Persson, K. A.; Ceder, G. The thermodynamic scale of inorganic crystalline metastability. *Sci. Adv.* **2016**, *2*, No. e1600225.
- (61) Yubuta, K.; Mori, T.; Okada, S.; Prots, Y.; Borrmann, H.; Grin, Y.; Shishido, T. High-Resolution Electron Microscopy and X-Ray Diffraction Study of Intergrowth Structures in α - and β -Type YbAlB_4 Single Crystals. *Philos. Mag.* **2013**, *93*, 1054–1064.
- (62) Liechtenstein, A. I.; Katsnelson, M. I.; Antropov, V. P.; Gubanov, V. A. Local spin density functional approach to the theory of exchange interactions in ferromagnetic metals and alloys. *J. Magn. Magn. Mater.* **1987**, *67*, 65–74.
- (63) Pashov, D.; Acharya, S.; Lambrecht, W. R. L.; Jackson, J.; Belashchenko, K. D.; Chantis, A.; Jamet, F.; van Schilfgaarde, M. Questaal: A package of electronic structure methods based on the linear muffin-tin orbital technique. *Comput. Phys. Commun.* **2020**, *249*, 107065.
- (64) Kato, T.; Oosawa, A.; Takatsu, K.; Tanaka, H.; Shiramura, W.; Nakajima, K.; Kakurai, K. Magnetic excitations in the spin gap system KCuCl_3 and TCuCl_3 . *J. Phys. Chem. Solids* **1999**, *60*, 1125–1128.
- (65) Zhu, M.; Matsumoto, M.; Stone, M. B.; Dun, Z. L.; Zhou, H. D.; Hong, T.; Zou, T.; Mahanti, S. D.; Ke, X. Amplitude modes in three-dimensional spin dimers away from quantum critical point. *Phys. Rev. Res.* **2019**, *1*, 033111.
- (66) Tanaka, H.; Takatsu, K. I.; Shiramura, W.; Ono, T. Singlet ground state and excitation gap in the double spin chain system KCuCl_3 . *J. Phys. Soc. Jpn.* **1996**, *65*, 1945–1948.
- (67) Vinnik, O.; Tarasenko, R.; Orendáč, M.; Orendáčová, A. Dimerized nature of magnetic interactions in the $S = 1/2$ quantum antiferromagnet $\text{Cu}(\text{en})_2\text{SO}_4$. *J. Magn. Magn. Mater.* **2022**, *547*, 168789.
- (68) Carlin, R. L.; van Duyneveldt, A. J. Dimers and clusters. *Magnetic Properties of Transition Metal Compounds*; Springer: Berlin, Heidelberg, 1977; pp 77–108.
- (69) Gamage, E. H.; Ribeiro, R. A.; Harmer, C. P.; Canfield, P. C.; Ozarowski, A.; Kovnir, K. Tuning of Cr-Cr Magnetic Exchange through Chalcogenide Linkers in Cr_2 Molecular Dimers. *Inorg. Chem.* **2022**, *61*, 6160–6174.
- (70) Tokuda, M.; Yubuta, K.; Shishido, T.; Sugiyama, K. Redetermination of the crystal structure of yttrium chromium tetraboride, YCrB_4 , from single-crystal X-ray diffraction data. *Acta Crystallogr., Sect. E: Crystallogr. Commun.* **2023**, *79*, 1072–1075.
- (71) Fokwa, B. P. T.; Samolyuk, G. D.; Miller, G. J.; Dronskowski, R. Ladders of a Magnetically Active Element in the Structure of the Novel Complex Boride $\text{Ti}_9\text{Fe}_2\text{Ru}_{18}\text{B}_8$: Synthesis, Structure, Bonding, and Magnetism. *Inorg. Chem.* **2008**, *47*, 2113–2120.
- (72) Brzoch, J.; Goerens, C.; Fokwa, B. P. T.; Miller, G. J. Scaffolding, Ladders, Chains, and Rare Ferrimagnetism in Intermetallic Borides: Electronic Structure Calculations and Magnetic Ordering. *J. Am. Chem. Soc.* **2011**, *133*, 6832–6840.
- (73) Goerens, C.; Brzoch, J.; Miller, G. J.; Fokwa, B. P. T. Scaffolding, Ladders, Chains, and Rare Ferrimagnetism in Intermetallic Borides: Synthesis, Crystal Chemistry and Magnetism. *Inorg. Chem.* **2011**, *50*, 6289–6296.
- (74) Blöchl, P. E. Projector augmented-wave method. *Phys. Rev. B: Condens. Matter Mater. Phys.* **1994**, *50*, 17953–17979.
- (75) Kresse, G.; Furthmüller, J. Efficient iterative schemes for ab initio total-energy calculations using a plane-wave basis set. *Phys. Rev. B: Condens. Matter Mater. Phys.* **1996**, *54*, 11169–11186.
- (76) Perdew, J. P.; Burke, K.; Ernzerhof, M. Generalized gradient approximation made simple. *Phys. Rev. Lett.* **1996**, *77*, 3865–3868.
- (77) Samolyuk, G. D.; Antropov, V. P. Character of magnetic instabilities in CaFe_2As_2 . *Phys. Rev. B: Condens. Matter Mater. Phys.* **2009**, *79*, 052505.